Journal of the Korean Astronomical Society
49: 127 ∼ 136, 2016 August
©2016. The Korean Astronomical Society. All rights reserved.
http://dx.doi.org/10.5303/JKAS.2016.49.4.127
pISSN: 1225-4614 · eISSN: 2288-890X
http://jkas.kas.org

Optical Properties of Amorphous Alumina Dust in the Envelopes around O-Rich AGB Stars

Kyung-Won Suh

Department of Astronomy and Space Science, Chungbuk National University, Cheongju 28644, Korea
kwsuh@chungbuk.ac.kr

Received June 22, 2016; accepted July 11, 2016

Abstract: We investigate optical properties of amorphous alumina (Al_2O_3) dust grains in the envelopes around O-rich asymptotic giant branch (AGB) stars using laboratory measured optical data. We derive the optical constants of amorphous alumina over a wide wavelength range that satisfy the Kramers-Kronig relation and reproduce the laboratory data. Using the amorphous alumina and silicate dust, we compare the radiative transfer model results with the observed spectral energy distributions. Comparing the theoretical models with observations on various IR two-color diagrams for a large sample of O-rich AGB stars, we find that the amorphous alumina dust (about 10-40%) mixed with amorphous silicate better models the observed points for the O-rich AGB stars with thin dust envelopes.

Key words: stars: AGB and post-AGB — dust: extinction — circumstellar matter — infrared: stars — radiative transfer

1. Introduction

The main site of dust formation is believed to be the cool envelopes around asymptotic giant branch (AGB) stars. O-rich AGB stars (M-type Miras and OH/IR stars) typically show conspicuous 10 μm and 18 μm features in emission or absorption suggesting the presence of amorphous silicate dust grains in the outer envelopes around them (Jones & Merrill 1976).

Low mass-loss rate O-rich AGB (LMOA) stars with thin dust envelopes show 10 μm and 18 μm emission features of amorphous silicate. High mass-loss rate O-rich AGB (HMOA) stars with thick dust envelopes show absorbing features at the same wavelengths (e.g., Suh 2004). Water-ice was found in some HMOA stars (Justtanont et al. 2006; Suh & Kwon 2013) and amorphous alumina (Al_2O_3) dust grains were detected in many LMOA stars (e.g., Sloan & Price 1998).

In a number of previous works (e.g., Markwick-Kemper et al. 2007; Suh & Kwon 2011), the term corundum was erroneously assigned to different kinds of solid alumina regardless of its crystal structure. However, only one of the crystalline Al_2O_3 polymorphs deserves the name corundum: namely α-Al_2O_3 which has trigonal lattice symmetry (e.g., Koike et al. 1995). While the amorphous aluminum oxide material (Al_2O_3) synthesized by Begemann et al. (1997) shows a single peak at 11.8 μm, corundum shows much sharper multiple peaks around 12 μm (Koike et al. 1995; Zeidler et al. 2013).

In this work, we investigate optical properties of amorphous alumina (Al_2O_3) dust in the envelopes around O-rich AGB stars. We derive the optical constants of the alumina dust in a wide wavelength range, which satisfy the Kramers-Kronig relation and reproduce the laboratory measured optical data. Using the opacity function of the amorphous alumina dust so obtained, we compare the theoretical radiative transfer model results with the observed spectral energy distributions (SEDs) and observations on various IR two-color diagrams (2CDs) for a large sample O-rich AGB stars.

Corresponding author: K.-W. Suh

2. Amorphous Alumina Dust

Dust opacity is determined by the shape and size of dust grains and its optical constants which are quantified by the complex index of refraction, $m(\lambda) = n(\lambda) + ik(\lambda)$, or complex dielectric function, $\varepsilon(\lambda) = \varepsilon_1(\lambda) + i\varepsilon_2(\lambda)$, where $\varepsilon = m^2$. We can derive $\varepsilon_1(\lambda)$ and $\varepsilon_2(\lambda)$ from the opacity function $Q_{ext}(\lambda)$ by imposing a supplementary physical constraint. Namely, the dielectric constants should satisfy the Kramers-Kronig relation (e.g., Bohren & Huffman 1983).

Silicate dust is believed to be the main dust species for O-rich AGB stars (Jones & Merrill 1976; Suh 1999). Alumina dust has been detected in the spectra of many LMOA stars in our Galaxy (Sloan & Price 1998; Speck et al. 2000) and the Large Magellanic Cloud (Jones et al. 2014). The shape of the 10 μm emission feature of LMOA stars, which is mainly produced by silicates, can be modified by addition of the alumina dust.

For LMOA stars, the broad 10 μm emission feature in $\lambda = 8-15$ μm is best fitted with a mixture of amorphous alumina and silicate dust. Egan & Sloan (2001), Suh & Kwon (2011), and Jones et al. (2014) found that the dust opacity using alumina dust as well as silicates can improve the model fit for a large sample of LMOA stars. They also found that the 10 μm absorption feature is likely to be produced by only silicate dust for HMOA stars.

Table 1
Models for amorphous alumina dust

Model	Laboratory Data[1]	K-K[2]	Usage[1]
model 1	Be97	Yes	This work
model 2	Be97; Ko95	Yes	-
model 3	Be97; Ko95	No	SK11; Jon14

[1]Be97: Begemann et al. (1997); Ko95: Koike et al. (1995); SK11: Suh & Kwon (2011); Jon14: Jones et al (2014), [2]K-K: the Kramers-Kronig relation.

Begemann et al. (1997; hereafter Be97) used laboratory measurements to determine the optical constants for amorphous alumina (Al_2O_3) in the wavelength range 7.8−500 μm. The alumina grains produce a single peak at 11.8 μm and influence the shape of the SED around 10 μm. The bulk density of the amorphous alumina was 3.2 g cm^{-3}.

Suh & Kwon (2011) and Jones et al. (2014) used the optical constants for amorphous (porous) alumina grains obtained by Be97 in the wavelength range 7.8−500 μm and extended them to the shorter wavelength range ($\lambda < 7.8$ μm) by concatenation with the optical constants of corundum dust measured by Koike et al. (1995; hereafter Ko95). However, the interpolated optical constants are not physically reliable because they are from different materials and also do not satisfy the Kramers-Kronig relation.

2.1. Deriving the Optical Constants

To obtain the complex dielectric functions, we have used the following procedure similar to that used in Suh (1999):

(i) $\varepsilon_2(\lambda)$ is adopted over a electromagnetic spectrum to agree with the existing laboratory data.

(ii) $\varepsilon_1(\lambda)$ is obtained using the Kramers-Kronig relation

$$\varepsilon_1(\lambda) = 1 + \frac{2}{\pi} P \int_0^\infty \frac{x\varepsilon_2(x)}{x^2 - \lambda^2} dx \qquad (1)$$

where P indicates the Cauchy principal value.

(iii) From the complex dielectric function, we calculate $\kappa_{abs}(\lambda)$. $\kappa_{abs}(\lambda)$ is compared with the desired opacity function.

(iv) In case of disagreements, the choice of $\varepsilon_2(\lambda)$ is modified, and steps (ii) - (iv) are repeated.

From the satisfactory sets of complex dielectric constants, we can calculate the optical constants ($m(\lambda) = n + ik$).

2.2. Models for Amorphous Alumina Dust

Figure 1 shows the opacity function (mass absorption coefficients) and complex dielectric constants for three different models of alumina dust. The opacity function of amorphous warm silicate (Suh 1999) is also displayed for comparison. Using Mie theory (Bohren & Huffman 1983), the opacity functions are calculated for uniform distribution of spherical dust grains with radius 0.1 μm. The opacity function for amorphous (porous) alumina dust measured by Be97 shows a single peak at 11.8 μm.

For model 1, we have derived the sets of complex dielectric constants in the wavelength range 0.1−3600 μm using the Kramers-Kronig procedures described in section 2.1. We use the same $\varepsilon_2(\lambda)$ in the wavelength range 7.8−500 μm as presented by Be97 for amorphous (porous) alumina (Al_2O_3). In other wavelength ranges, we have chosen $\varepsilon_2(\lambda)$ so that the calculated $\varepsilon_1(\lambda)$ in the wavelength range 7.8−500 μm matches the data presented by Be97. Small deviations of $\varepsilon_1(\lambda)$ around the end points (7.8 and 500 μm) were not avoidable. In the short (0.1−7.8μm) wavelength range, where the laboratory data are not available, the opacity function is similar to that of silicate dust. In the longer (500−3600 μm) wavelength end, where the laboratory data are not available, the opacity function obeys approximately a simple power law ($\kappa_{abs} \propto \lambda^{-2}$) just like silicate dust.

For model 2, we use $\varepsilon_2(\lambda)$ from Be97 (amorphous porous alumina) in the wavelength range 7.8−500 μm and $\varepsilon_2(\lambda)$ from Ko95 (corundum) in the short wavelength range ($\lambda < 7.8$ μm). $\varepsilon_1(\lambda)$ is calculated from the combined $\varepsilon_2(\lambda)$ using the Kramers-Kronig relation. Because of the small change of $\varepsilon_2(\lambda)$ from model 1 in $\lambda < 7.8$ μm (see the lower panel of Figure 1), the calculated $\varepsilon_1(\lambda)$ and opacity function for model 2 in the wavelength range 7.8−500 μm are very different from those for model 1 (or Be97). Model 2 would not be physically reliable because the complex dielectric constants are from different materials.

For model 3, the optical constants (n and k) for amorphous (porous) alumina grains obtained by Be97 are extended to the shorter wavelength range ($\lambda <$ 7.8 μm) by concatenation with the optical constants of corundum measured by Ko95. $\varepsilon_2(\lambda)$ is the same as the one from Ko95, but $\varepsilon_1(\lambda)$ shows some deviations in the range $\lambda < 7.8$ μm (see Figure 1) because of differences in the two sets of optical constants (Be97 and Ko95) at 7.8 μm. Compared with model 2, model 3 shows the same $\varepsilon_2(\lambda)$ but different $\varepsilon_1(\lambda)$. This model was used by Suh & Kwon (2011) and Jones et al. (2014). Because the interpolated optical constants are from different materials and do not satisfy the Kramers-Kronig relation, model 3 would also not be physically reliable.

Table 1 summarizes properties of the three models. Even though the three models can reproduce the observations in similar ways, it is meaningless to use physically unreliable models for amorphous alumina because other dust species could also produce similar features in the wavelength range. Therefore, we use only model 1 for amorphous alumina dust in this work.

3. RADIATIVE TRANSFER MODEL CALCULATIONS

We use the radiative transfer code DUSTY developed by Ivezić & Elitzur (1997) for a spherically symmetric dust shell. We have performed the model calculations in the wavelength range 0.1 to 3600 μm. For all models, we assume the dust density distribution is continuous ($\rho \propto r^{-2}$). The outer radius of the dust shell is always taken to be 10^4 times the inner radius (R_c). We choose 10 μm as the fiducial wavelength that sets the scale of

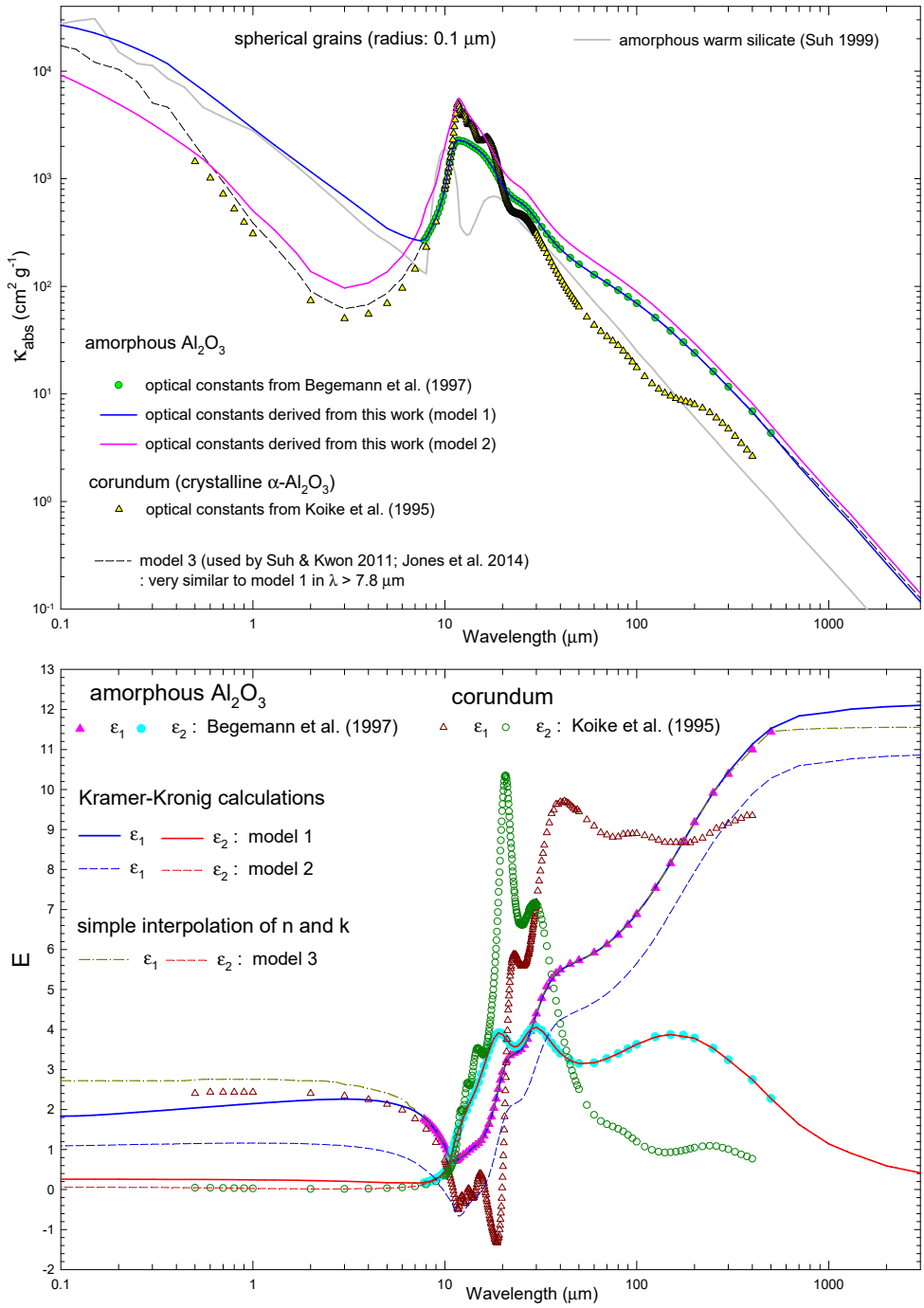

Figure 1. Opacity functions and indices of refraction of for alumina dust.

the dust optical depth (τ_{10}). For the central star, we assume that the luminosity is 10^4 $L_\odot$ for all models.

For dust opacity, we use a simple mixture of silicate and alumina (10−40% by number) dust grains as well as pure silicates. For silicate dust, we use the optical constants of warm and cold silicate grains derived by Suh (1999). We use the warm silicate dust for LMOA stars (models with $\tau_{10} \leq 3$) and the cold silicate dust for HMOA stars (models with $\tau_{10} > 3$). For alumina dust, we use the optical constants of amorphous alumina derived from this work (model 1; see Section 2.2) based on the laboratory data from Be97. As mentioned earlier, we assume that all dust grains are spherical with a uniform radius of 0.1 μm.

3.1. Typical Model SEDs

The upper panel of Figure 2 shows the typical model SEDs for LMOA stars. The lower panel of Figure 2 shows the typical model SEDs for HMOA stars. They show the theoretical model SEDs using a simple mixture

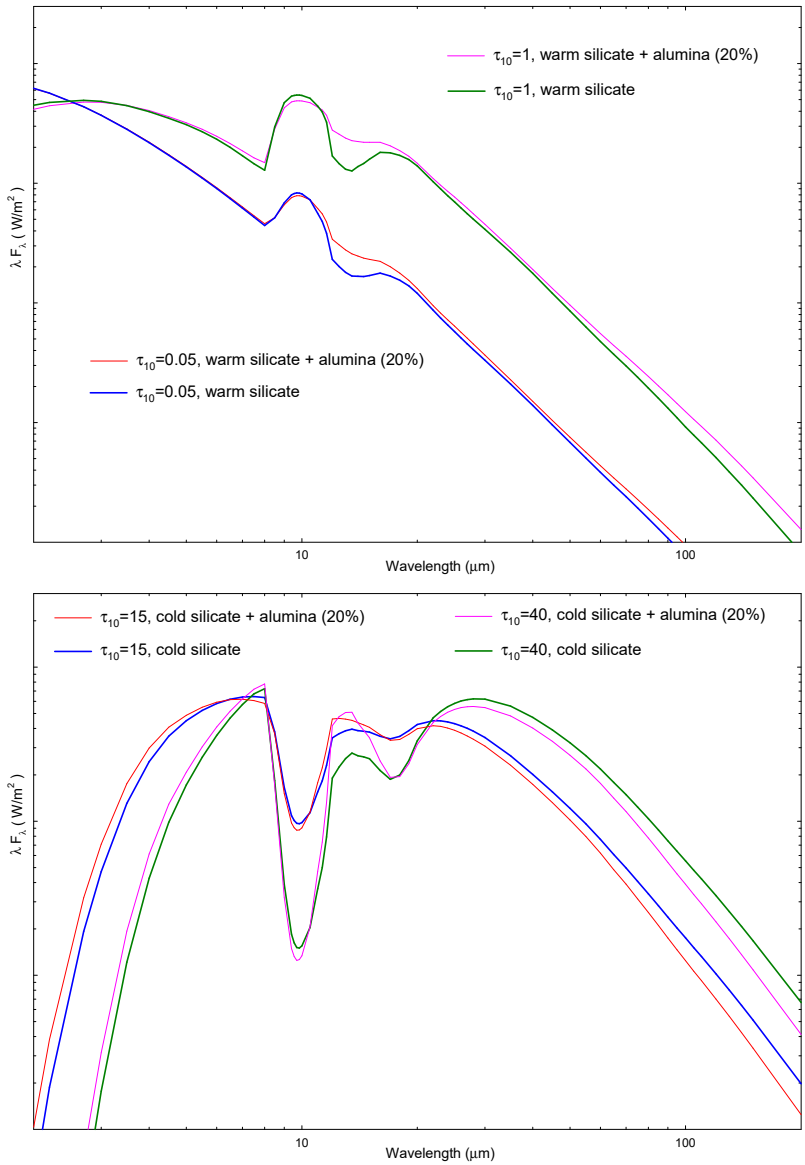

Figure 2. Theoretical model SEDs for O-rich AGB stars.

of silicate and alumina dust as well as pure silicates. We assume that the stellar blackbody temperature is 2500 K for LMOA stars and 2000 K for HMOA stars. The dust condensation temperature (T_c) is assumed to be 1000 K.

3.2. Comparison of the Model SEDs with the Observations

In Figures 3 and 4, we compare the theoretical model SEDs with the observed SEDs for two LMOA stars (omi Cet and Z Cyg) and two HMOA stars (OH 127.8+0.0 and OH 21.5+0.5). For the objects, the spectral data from the Infrared Space Observatory (ISO) and Infrared Astronomical Satellite (IRAS) Low Resolution Spectrograph (LRS; $\lambda = 8-22$ μm) are used. We use the ISO data from the Short Wavelength Spectrometer (SWS; $\lambda = 2.4-45.4$ μm) and Long Wavelength Spectrometer (LWS; $\lambda = 43-197$ μm). We also use the photometric data from the IRAS Point Source Catalog (PSC) and AKARI (Murakami et al. 2007).

For LMOA stars, the stellar blackbody temperature is assumed to be 2500 K and 2650 for omi Cet and Z Cyg, respectively. The dust condensation temperature (T_c) is assumed to be 654 K and 463 K for omi Cet and Z Cyg, respectively. Suh (2004) pointed out that T_c looks to be low (400−800 K) for LMOA stars with thin dust envelopes.

For both LMOA stars, a mixture of amorphous alumina with silicate dust grains produces different model SEDs compared to the model SEDs produced by pure silicate dust in $\lambda = 8-20$ μm. The mixture of amorphous alumina dust reproduces the observed SEDs better in $\lambda = 11-15$ μm. Other important dust species such as MgFeO series may need to be included to obtain a better fit. The dust grains of MgFeO series produce

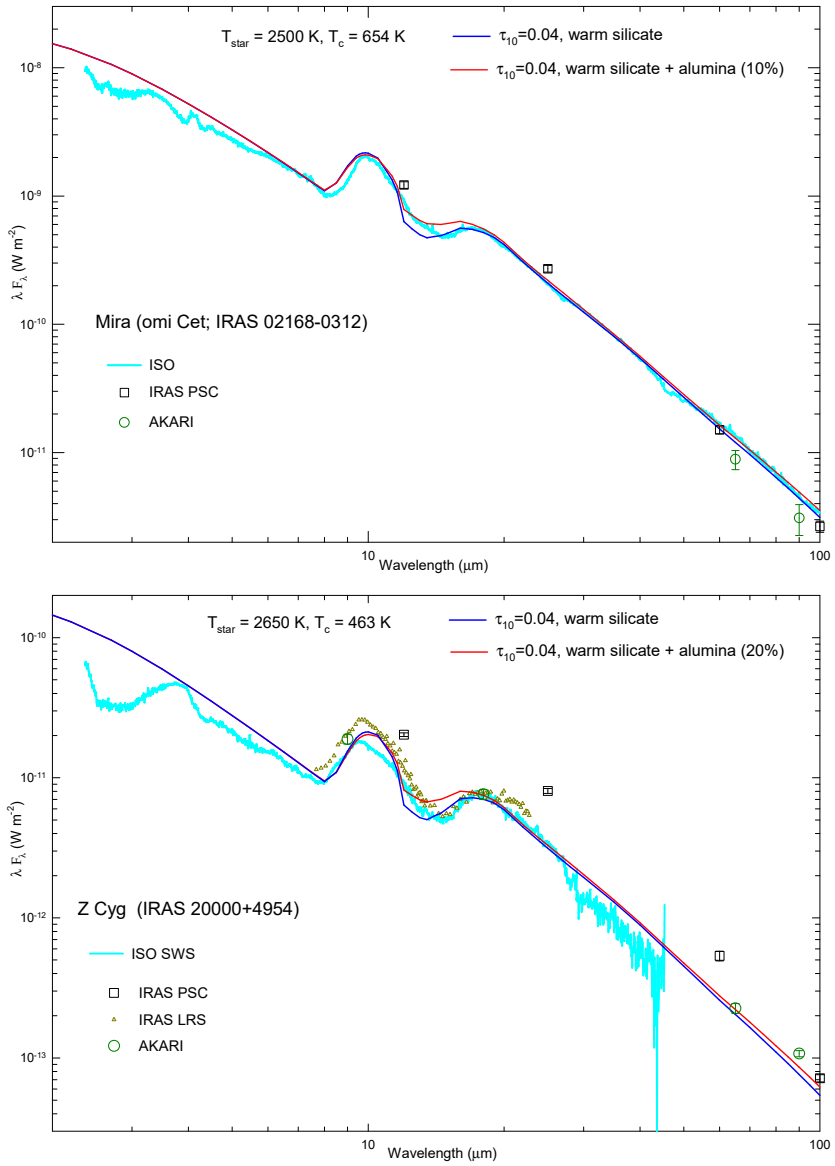

Figure 3. Model SEDs compared with the observed SEDs for LMOA stars.

single peaks in λ = 15-22 μm (Henning et al. 1995).

In Figure 4, the observed SEDs are compared with the theoretical model SEDs for HMOA stars. For the two HMOA stars, we find that the amorphous alumina dust is not useful to reproduce the observed SEDs. For both objects, the stellar blackbody temperature is assumed to be 2000 K and T_c is assumed to be 1000 K.

4. IR 2CDs for O-Rich AGB Stars

IR 2CDs are useful to characterize the dust envelopes around AGB stars and post-AGB stars (e.g., Suh 2015). Suh & Kwon (2011) presented a list of AGB stars for 3003 O-richstars in our Galaxy and Kwon & Suh (2012) presented a revised sample of 3373 O-rich AGB stars.

For these stars, we obtain photometric data in three bands (12, 25, and 60 μm) by using version 2.1 of the IRAS PSC. We also use the AKARI PSC data in two bands (9 and 18 μm) obtained by the infrared camera, Two Micron All Sky Survey (2MASS; Cutri et al. 2003) data in K_s (2.159 μm) band, and Midcourse Space Experiment (MSX; Egan et al. 2003) data in four broad bands centered at 8.28, 12.13, 14.65, and 21.34 μm. We cross-identify the AKARI, 2MASS, and MSX sources by finding the nearest one from the IRAS PSC position.

The color index is defined by

$$M_{\lambda 1} - M_{\lambda 2} = 2.5 \log_{10} \frac{F_{\lambda 2}/ZMC_{\lambda 2}}{F_{\lambda 1}/ZMC_{\lambda 1}} \qquad (2)$$

where $ZMC_{\lambda i}$ means the zero magnitude calibration at given wavelength (λi) (see Suh & Kwon 2011 for details). We use only those objects with good quality data at any wavelength.

Figures 5 and 6 show the IR 2CDs for the 3373 O-rich AGB stars compared with theoretical models. The

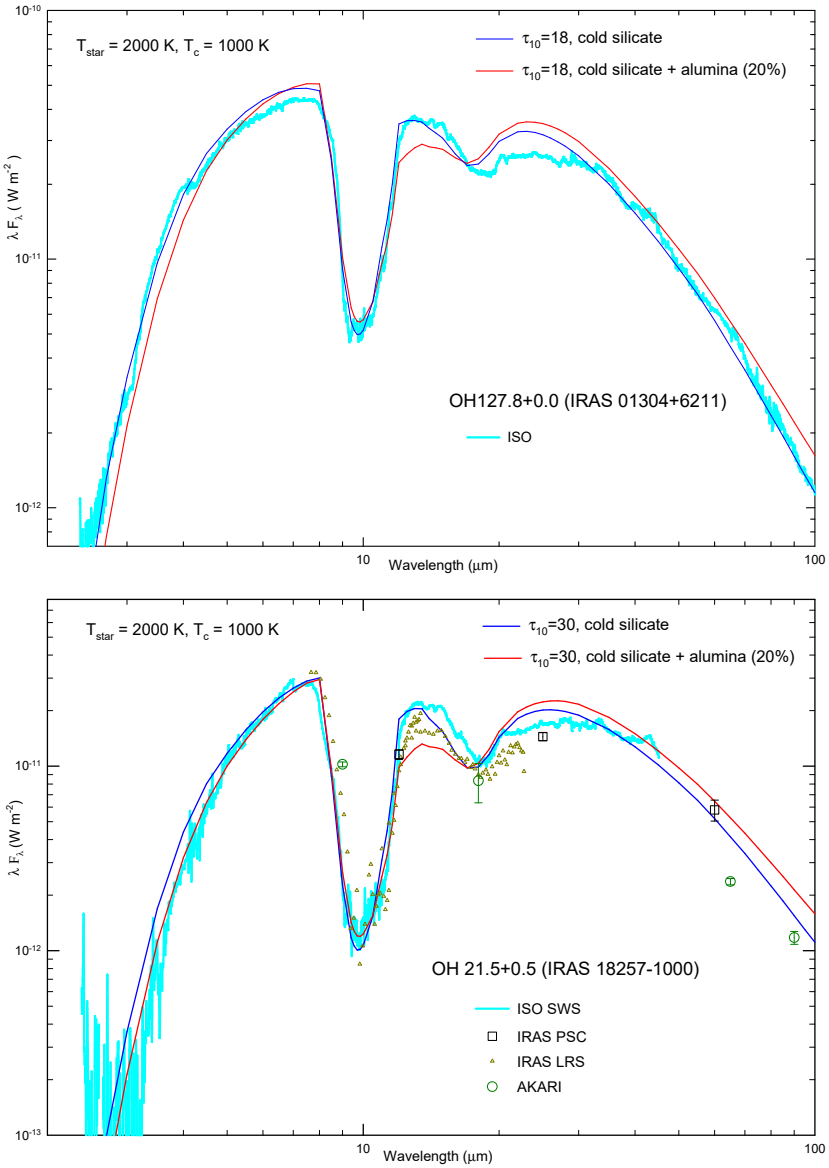

Figure 4. Model SEDs compared with the observed SEDs for HMOA stars.

small symbols are observational data and the lines with large symbols are theoretical model calculations for a range of optical depths of the dust shell. These models are explained in Section 4.1. Generally, the stars in the upper-right region of the 2CDs have thick dust shells with large optical depths.

4.1. Theoretical Models for the 2CDs

Using the radiative transfer model for the dust shells as explained in Section 3, we perform model calculations for eleven optical depths (τ_{10} = 0.005, 0.01, 0.05, 0.1, 0.5, 1, 3, 7, 15, 30, and 40). We assume that the stellar blackbody temperature is 2500 K for $\tau_{10} \leq 3$ and 2000 K for $\tau_{10} > 3$. The dust condensation temperature (T_c) is assumed to be 500 K and 1000 K.

We use the warm silicate dust for LMOA stars (7 models with $\tau_{10} \leq 3$) and cold silicate dust for HMOA stars (4 models with $\tau_{10} > 3$). We also show the models using a simple mixture of silicate and alumina (20−40%) dust.

4.2. Comparison on 2CDs

Figures 5 and 6 show the IRAS, IRAS-NIR, MSX, IRAS-AKARI 2CDs for O-rich AGB stars compared with the theoretical models. LMOA stars are located in the lower-left region and HMOA stars are located in the upper-right region (lower-right region for the MSX 2CD) in all 2CDs. Generally, we find that the basic theoretical model tracks roughly coincide with the densely populated observed points.

The theoretical model tracks are shown for dust condensation temperatures (T_c) of 500 K and 1000 K. Suh (2004) pointed out that a lower T_c (T_c < 1000 K) is required for LMOA stars with thin dust envelopes. Generally, we find that the models with a higher T_c (1000 K) reproduce the observations of HMOA stars

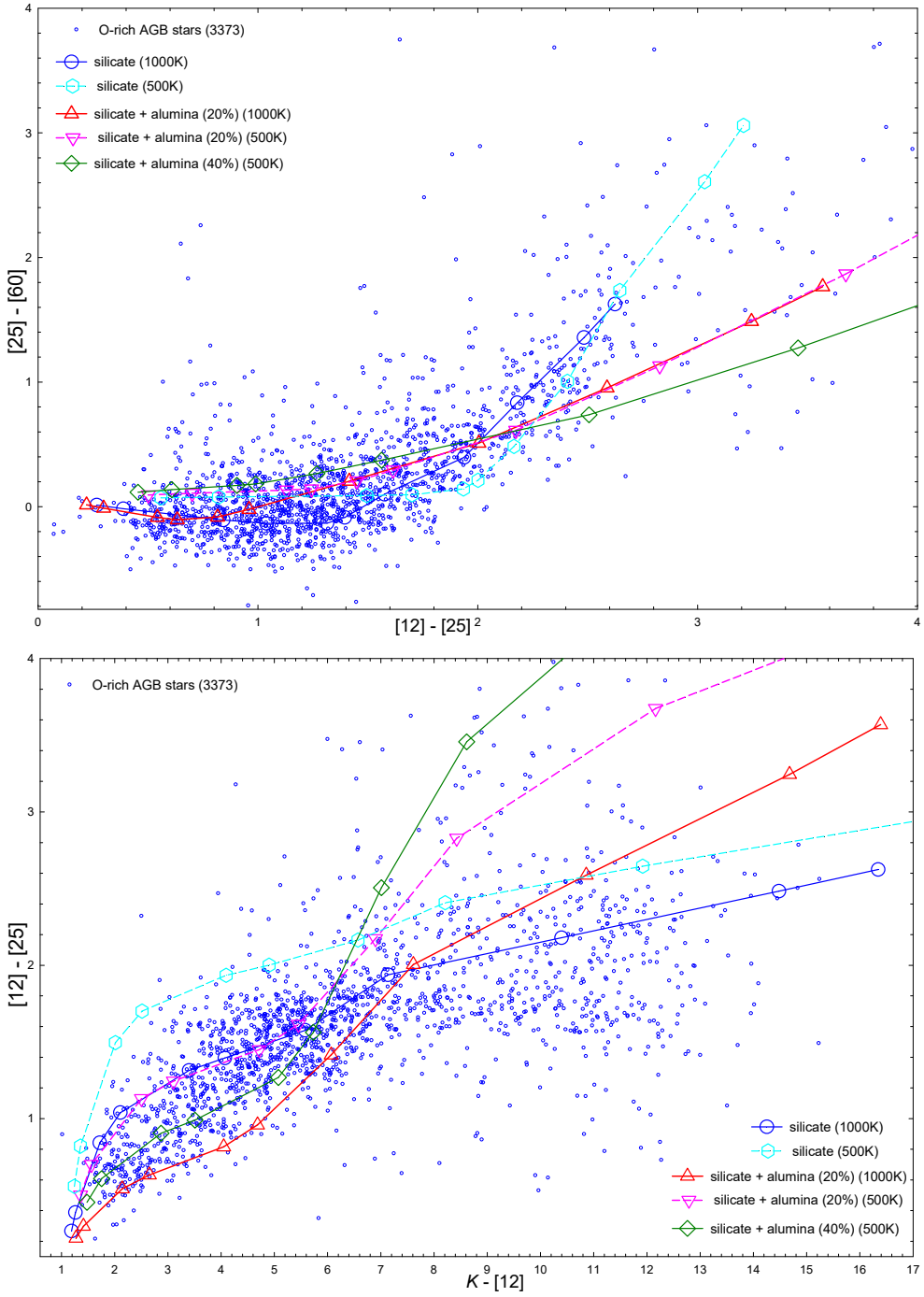

Figure 5. IR 2CDs for O-rich AGB stars compared with theoretical dust shell models (from left to right: τ_{10} = 0.005, 0.01, 0.05, 0.1, 0.5, 1, 3, 7, 15, 30, and 40).

better while the models with a lower T_c (500 K) reproduce the observations of LMOA stars better for most 2CDs.

The shape of the 10 μm feature of O-rich AGB stars, which is mainly produced by silicate, can be modified by addition of the alumina dust. Because amorphous alumina dust produces a single peak at 11.8 μm, the AKARI, IRAS, and MSX fluxes at 9, 8.28, 12, and 14.65 μm would be easily affected by the alumina dust. The dust grains of MgFeO series (Henning et al. 1995) produce single peaks in λ 15-22 μm which could be responsible for the MSX flux at 14.65 and 21.34 μm. The models with pure silicate dust opacity do not result in satisfactory fits for some 2CDs possibly because of the presence of alumina and MgFeO series dust.

The upper panel of Figure 5 plots AGB stars in an IRAS 2CD using [25]−[60] versus [12]−[25]. The model lines using a mixture of alumina are different

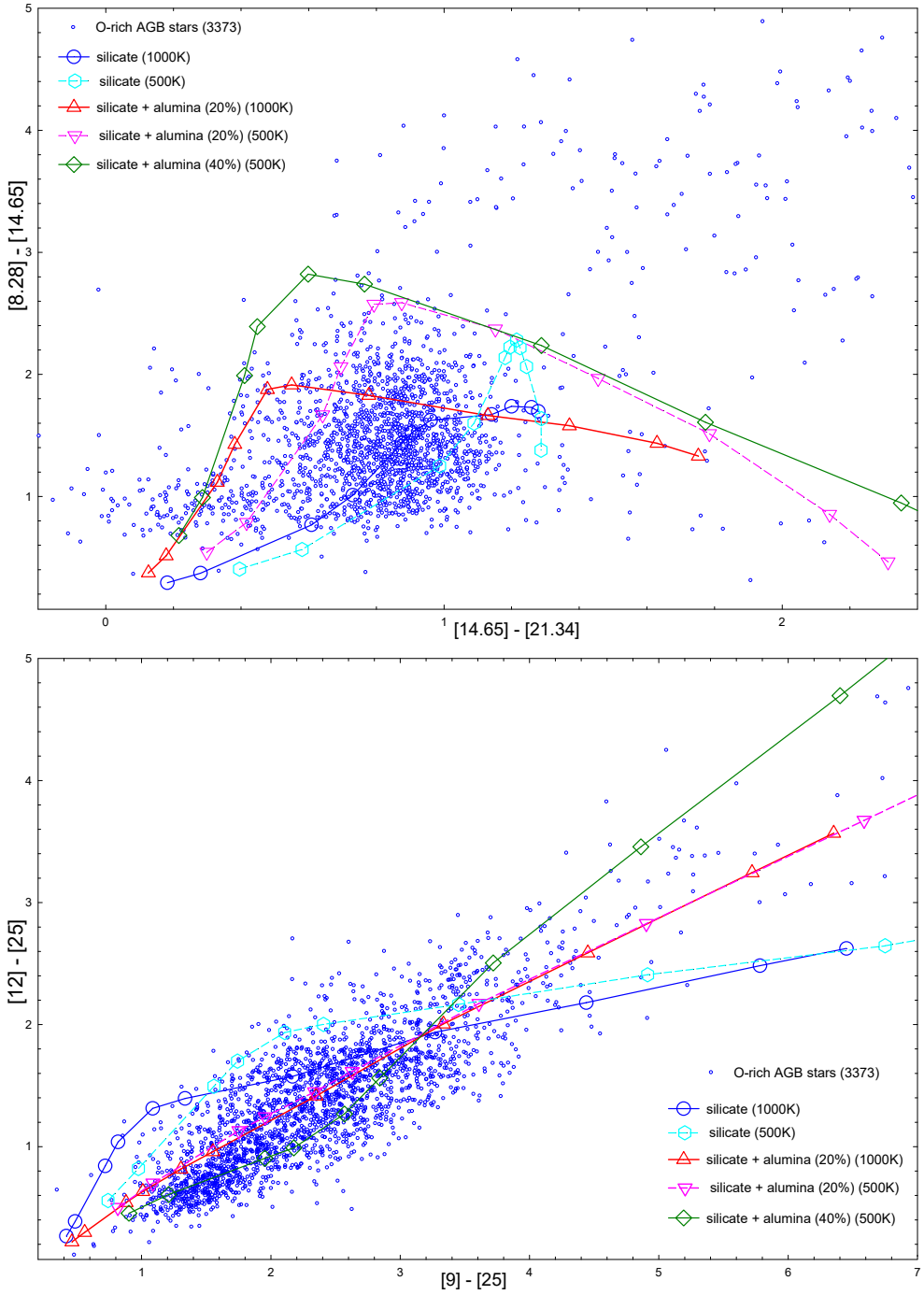

Figure 6. IR 2CDs for O-rich AGB stars compared with theoretical dust shell models (from left to right: τ_{10} = 0.005, 0.01, 0.05, 0.1, 0.5, 1, 3, 7, 15, 30, and 40).

from those using pure silicate because the IRAS flux at 12 μm is affected by addition of alumina dust. For HMOA stars, the alumina models are not useful because they produce exceedingly large [12]−[25] colors because the alumina dust modifies the 10 μm silicate absorption feature resulting in the smaller flux at 12 μm.

The lower panel of Figure 5 shows an IRAS-NIR 2CD using [12]−[25] versus K−[12]. For LMOA stars, the alumina models are very useful because they produce smaller [12]−[25] colors because the alumina dust modifies the 10 μm silicate emission feature resulting in the larger flux at 12 μm. The alumina models can easily reproduce the LMOA stars in the lower-left region of the 2CD.

The upper panel of Figure 6 shows a MSX 2CD using [8.28]−[14.65] versus [14.65]−[21.34]. The MSX fluxes at 14.65 μm are affected by the alumina dust. The alumina models can reproduce the LMOA stars

in the upper-left region because the [8.28]−[14.65] colors become redder (or larger) due to the alumina dust, which produces more emission at 14.65 μm (see the upper panel of Figure 2).

On the MSX 2CD, the theoretical model points for very large dust optical depths are located in lower-right region, unlike other 2CDs. This is because the [8.28]−[14.65] colors become bluer (or smaller) for large dust optical depths due to the deep silicate absorption feature at 18 μm, which lowers the flux at 14.65 μm relative to the flux at 8.28 μm (see the lower panel of Figure 2). The objects in the upper-right region could be post-AGB stars (see Suh 2015).

The lower panel of Figure 6 shows an AKARI-IRAS 2CD using [12]−[25] versus [9]−[25]. This 2CD shows the largest deviations of the theoretical models from the observations because of the AKARI flux at 9 μm. Similar effects were noticed in Suh & Kwon (2011). The observed points in the lower-left region of the 2CD can be reproduced by the theoretical models using the larger alumina contents (40-50%), compared with other 2CDs.

For all IR 2CDs, we find that the amorphous alumina dust is useful only for LMOA stars with thin dust envelopes which show the silicate emission features at 10 and 18 μm.

5. Summary

In this work, we have investigated optical properties of the amorphous alumina (Al_2O_3) dust grains in the envelopes around O-rich AGB stars, utilizing laboratory measured optical data. We have derived the the optical constants of the amorphous alumina dust in a wide wavelength range, that satisfy the Kramers-Kronig relation and reproduce the laboratory measured data.

Amorphous alumina grains produce a single peak at 11.8 μm and influences the shape of the SED at around 10 μm. The shape of the 10 μm feature of O-rich AGB stars, which is mainly produced by silicate, can be modified by addition of the alumina dust. Using the opacity function of the alumina dust, we have compared the theoretical radiative transfer model results with the observed SEDs and observations on various IR 2CDs for a large sample O-rich AGB stars.

Even though it is difficult to suggest the exact content of amorphous alumina for O-rich AGB stars because dust species other than alumina can also produce similar features in the wavelength range 8-15 μm, we have found a general trend for a large sample of the stars on 2CDs. Comparing the theoretical models with the observations on various IR 2CDs, we have found that the amorphous alumina dust (about 10-40%) mixed with amorphous silicate can reproduce many more observed points for LMOA stars, which have thin dust envelopes. Because alumina dust is not useful for HMOA stars, we expect that the relative alumina abundance for LMOA stars is higher than the abundance for HMOA stars with thick dust envelopes.

We expect that the optical constants for amorphous alumina derived in this work will be useful for further studies on dust around AGB and post-AGB stars. The optical constants for the amorphous alumina derived in this work will be accessible through the author's web site: `http://web.chungbuk.ac.kr/~kwsuh/d-opt.htm`.

Acknowledgments

This research was supported by Basic Science Research Program through the National Research Foundation of Korea (NRF) funded by the Ministry of Science, ICT & Future Planning (NRF-2013R1A1A2057841). This work was supported by the intramural research grant of Chungbuk National University in 2015.

References

Begemann, B., Dorschner, J., Henning, T., et al. 1997, Aluminum Oxide and the Opacity of Oxygen-Rich Circumstellar Dust in the 12-17 Micron Range, ApJ, 476, 199

Bohren C. F., & Huffman D. R. 1983, Absorption and Scattering of Light by Small Particles (New York: Wiley)

Cutri, R. M., Skrutskie, M. F., Van Dyk, S., et al. 2003, VizieR Online Data Catalog: 2MASS All-Sky Catalog of Point Sources

Egan, M. P., Price, S. D., Kraemer, K. E., et al. 2003, VizieR Online Data Catalog: MSX6C Infrared Point Source Catalog

Egan, M. P., & Sloan, G. C. 2001, The Physical Basis for the Silicate Dust Sequence, ApJ, 558, 165

Henning, T., Begemann, B., Mutschke, H., & Dorschner J. 1995, Optical Properties of Oxide Dust Grains, A&AS, 112, 143

Ivezić, A., & Elitzur, M. 1997, Self-Similarity and Scaling Behaviour of Infrared Emission from Radiatively Heated Dust - I. Theory, MNRAS, 287, 799

Jones, O. C., Kemper, F., Srinivasan, S., et al. 2014, Modelling the Alumina Abundance of Oxygen-Rich Evolved Stars in the Large Magellanic Cloud, MNRAS, 440, 631

Jones, T. W., & Merrill, K. M. 1976, Model Dust Envelopes around Late-Type Stars, ApJ, 209, 509

Justtanont, K., Olofsson, G., Dijkstra, C., & Meyer, A. W. 2006, Near-Infrared Observations of Water-Ice in OH/IR Stars, A&A, 450, 1051

Koike, C., Kaito, C., Yamamoto, T., Shibai, H., Kimura, S., & Suto, H. 1995, Extinction Spectra of Corundum in the Wavelengths from UV to FIR, Icarus, 114, 203

Kwon, Y.-J., & Suh, K.-W. 2012, Properties of OH, SiO, and H_2O Maser Emission in O-Rich AGB Stars, JKAS, 45, 139

Markwick-Kemper, F., Gallagher, S. C., Hines, D. C., & Bouwman, J. 2009, Dust in the Wind: Crystalline Silicates, Corundum, and Periclase in PG 2112+059, ApJ, 668. L107

Murakami, H., Baba, H., Barthel, P., et al. 2007, The Infrared Astronomical Mission AKARI, PASJ, 59, 369

Sloan, G. C., & Price, S. D. 1998, The Infrared Spectral Classification of Oxygen-Rich Dust Shells, ApJS, 119, 141S

Speck, A. K., Barlow, M. J., Sylvester, R. J., & Hofmeister, A. M. 2000, Dust Features in the 10 μm Infrared Spectra of Oxygen-Rich Evolved Stars, A&AS, 146, 437

Suh, K.-W. 1999, Optical Properties of the Silicate Dust Grains in the Envelopes around Asymptotic Giant Branch Stars, MNRAS, 304, 389

Suh, K.-W. 2004, Pulsation Phase-Dependent Dust Shell Models for Oxygen-Rich Asymptotic Giant Branch Stars, ApJ, 615, 485
Suh, K.-W. 2015, Infrared Two-Color Diagrams for AGB Stars, Post-AGB Stars, and Planetary Nebulae, ApJ, 808, 165
Suh, K.-W., & Kwon, Y.-J. 2011, Infrared Two-Colour Diagrams for AGB Stars Using AKARI, MSX, IRAS and Near-Infrared Data, MNRAS, 417, 3047
Suh, K.-W., & Kwon, Y.-J. 2013, Water Ice in High Mass-Loss Rate OH/IR Stars, ApJ, 762, 113
Zeidler, S., Posch, T., & Mutschke, H. 2013, Optical Constants of Refractory Oxides at High Temperatures. Mid-Infrared Properties of Corundum, Spinel, and Alpha-Quartz, Potential Carriers of the 13 μm Feature, A&A, 553, 81